Influence of the statistical shift of Fermi level on the conductivity behavior in microcrystalline silicon

Sanjay K. Ram,[1,*] Satyendra Kumar,[1,†] and P. Roca i Cabarrocas[2]
[1]*Department of Physics, Indian Institute of Technology Kanpur, Kanpur-208016, India*
[2]*LPICM, UMR 7647–CNRS–Ecole Polytechnique, 91128 Palaiseau Cedex, France*
(Received 28 April 2007; revised manuscript received 28 December 2007; published 31 January 2008)

The electrical conductivity behavior of highly crystalline undoped hydrogenated microcrystalline silicon (μc-Si:H) films having different microstructures was studied. The dark conductivity is seen to follow the Meyer Neldel rule (MNR) in some films and anti-MNR in others, depending on the details of microstructural attributes and corresponding changes in the effective density of state distributions. A band tail transport and statistical shift of the Fermi level are used to explain the origin of MNR as well as anti-MNR in our samples. We present the evidence of anti-MNR in the various experimental transport data of μc-Si:H materials reported in literature and analyze these data together with ours to show the consistency and physical plausibility of the statistical shift model. The calculated MNR parameters and other significant material parameters derived therefrom are tenable for a wide microstructural range of the μc-Si:H system.

DOI: 10.1103/PhysRevB.77.045212 PACS number(s): 73.50.−h, 71.23.−k, 73.61.Jc, 61.72.Mm

I. INTRODUCTION

Measurement of electrical conductivity as a function of temperature is a tool conventionally used to study the electrical transport behavior of disordered systems where an exponential relationship is observed between the conductivity prefactor (σ_0) and the conductivity activation energy (E_a), known as the Meyer-Neldel rule (MNR or the compensation law).[1] The relationship is expressed as

$$\sigma_0 = \sigma_{00} e^{GE_a}, \tag{1}$$

where G and σ_{00} are called MN parameters. Often G^{-1} is denoted as E_{MN}, the Meyer-Neldel characteristic energy. MNR is a phenomenon seen in many thermally activated processes, including electronic conduction in amorphous silicon (a-Si:H). However, the microscopic origin of the MNR and the physical meaning of G are still a topic of discussion. Various theories have been put forward to explain the observed MNR in a-Si:H,[2,3] the most popular among these being the model invoking a statistical shift of the Fermi level (E_F) with temperature.[4–10] In contrast to the homogeneous a-Si:H, hydrogenated microcrystalline silicon (μc-Si:H) is a heterogeneous material consisting of a microcrystallite phase that is comprised of grains which conglomerate to form columns, and an amorphous (or disordered) phase and voids populating the intergrain and intercolumnar boundaries.[11–13] MNR has been reported in *doped* μc-Si:H films with MNR parameters similar to those obtained in a-Si:H,[14] which was explained in terms of the statistical shift model analogous to a-Si:H, and this formed the basis of several reports that treated the transport in μc-Si:H at par with a-Si:H. This led to the general belief that while the optical properties of μc-Si:H are governed by the crystalline component, the electrical transport is still controlled by the amorphous silicon phase.

Any analogy that does exist between μc-Si:H and a-Si:H materials gets somewhat undermined in the newer high mobility μc-Si:H materials having complete crystallization from the beginning of film growth.[15–19] In such a material, the absence of an amorphous phase gives rise to mechanisms and routes of electrical transport different from our conventional understanding of relationship between electrical transport and variation in crystallinity.[19] Apart from MNR, another interesting and important phenomenon, the anti-MNR, has been reported in heavily doped μc-Si:H (Refs. 20–22) and heterogeneous Si (het-Si) thin film transistors (TFTs).[23] A negative value of MN energy E_{MN} is seen in the case of anti-MNR. This phenomenon has been explained by the E_F moving deep into the band tail. Anti-MNR is not seen in a-Si:H, the accepted reason being that it is difficult to dope a-Si:H heavily enough to move E_F deeply into the tail DOS due to disorder induced broadening of the tail state distribution.

Therefore, the observation of MNR and anti-MNR in the electrical transport behavior of μc-Si:H draws our attention toward the basic physics in terms of both the origin and the significance of these relationships. In spite of the immense potential of high efficiencies and large area deposition capabilities shown by μc-Si:H in semiconductor technology, especially in photovoltaics[24,25] and TFTs,[26] the understanding of its transport properties is impeded by these lacunae. Different conduction mechanisms and paths have been invoked to explain the electrical transport behavior in μc-Si:H, deriving information that correlates some microstructural features and mechanisms. Azulay *et al.* have discussed such models.[19] However, the present approach does not provide an insight into what occurs at the electronic level, the knowledge of which could present a more unified picture of the electronic transport. The inherent microstructural complexities, the consequent intricacy of electrical transport behavior of this heterogeneous material, and the lack of knowledge regarding a reproducible relationship between the two continues to remain an obstacle to a clear view of the composite picture. The unavailability of an effective density of states (DOS) map of the heterogeneous μc-Si:H system contributes to the problem.

In this paper, we present the results of dark conductivity (σ_d) measurements (above room temperature) conducted on

a large number of well-characterized μc-Si:H samples having a broad range of microstructural features. In particular, fully crystalline μc-Si:H films without an amorphous tissue have been studied. In Sec. II, the experimental details are described. In Sec. III, we present the results of our measurements, which evince the occurrence of both MNR and anti-MNR in undoped μc-Si:H. We have discussed these findings in the context of statistical shift models in Sec. IV, where we show that these phenomena are intricately linked to the underlying microstructure and the corresponding DOS features of the material.[27] Further, a number of published temperature dependent conductivity data have been analyzed in a consistent framework. The conclusions are presented in Sec. V.

II. EXPERIMENT

The undoped μc-Si:H films were deposited at low substrate temperature ($T_s \leqslant 200$ °C) in a parallel-plate glow discharge plasma enhanced chemical vapor deposition system operating at a standard rf frequency of 13.56 MHz, using high purity SiF_4, Ar, and H_2 as feed gases. Different microstructural series of samples were created by systematically varying gas flow ratios ($R = SiF_4/H_2$) or T_s (100–250 °C) for samples having different thicknesses ($\approx$50–1200 nm). We employed bifacial Raman scattering (RS) (from film and substrate side), spectroscopic ellipsometry (SE), x-ray diffraction (XRD), and atomic force microscopy (AFM) for structural investigations. Many of the μc-Si:H films used in this study have been characterized by the time resolved microwave conductivity (TRMC) measurements as well. Coplanar $\sigma_d(T)$ measurements were carried out from 300 to 450 K on these well-characterized annealed samples having a variety of film thicknesses and microstructures and were studied in the context of deposition parameters.[27] At above room temperature, $\sigma_d(T)$ of all the μc-Si:H films having different microstructures, prepared under different deposition conditions, follows an Arrhenius-type thermally activated behavior,

$$\sigma_d = \sigma_0 e^{-E_a/kT}. \quad (2)$$

III. RESULTS

A systematic study and analyses of the results of the large number and variety of samples in this study necessitate organizing them into some classes having common attributes. Therefore, on the basis of structural investigations of the μc-Si:H films at various stages of growth and under different growth conditions, we have segregated out the unique features of microstructure and growth type present in the varieties of films, with respect to the correlative coplanar electrical transport properties, and have classified them into three types: *A*, *B*, and *C*. Since this classification is fundamental to this work, we first describe it here briefly. The classification has been described in our previous works and in more detail in some work communicated elsewhere.

An important concern that arises when we embark on such a classification is the choice of microstructural parameter that can be correlated to the observed electrical transport behavior. Deposition parameters only have an indirect causal link to the electrical properties through their primary effect on the microstructure of the material. In the beginning, we had attempted to correlate the classification to *thickness*, as a particular type of electrical transport behavior appeared to exist over a certain range of thickness (*type-A* behavior up to $\approx$350–400 nm, *type-B* behavior in the range of 400–900 nm, and *type-C* behavior above 900 nm).[28] However, the observed electrical transport behaviors could not be explained solely based on thickness, and each time we had to resort to a correlation between the growth stage of the film and the underlying film microstructure that could give rise to the observed electrical transport behavior. The growth stage of the film and the associated microstructural features do not correlate well to the *film thickness*, as they are influenced by the different deposition parameters.[18,27,28]

The μc-Si:H films under study demonstrated the presence of a crystallite size distribution, and the finding of SE studies showed the presence of large and small crystallite grains [(LG) and (SG), respectively], which is well corroborated by the deconvolution of RS profiles using a bimodal size distribution of large crystallite grains (LG $\approx$70–80 nm) and small crystallite grains (SG$\approx$6–7 nm). We have described the microstructure findings in detail a little further on. Returning to the final choice of microstructural parameter, we found that the percentage fraction of the LG (as deduced from SE, denoted by F_{cl}) showed a good correlation to the film microstructure of different μc-Si:H films, regardless of the thickness or deposition parameters.[18] Similarly, for films having similar microstructures and electrical transport behavior, the F_{cl} values were found to fall into similar ranges.[28] An extensive study comprising of a large number of samples having different thicknesses and microstructures, deposited under different conditions, showed that rather than film thickness or any other deposition parameter, the F_{cl} value could indicate well the microstructural and morphological stage of the μc-Si:H film and correlates well, albeit empirically, with the electrical transport behavior. We have few samples in this study having thicknesses that could belong to a certain type in a classification system based on thickness, but the observed electrical transport behaviors were not correlative with the "thickness zone" category in these samples.[28] The electrical transport behaviors were rather correlative with the F_{cl} range each sample falls in, and the classification based on such F_{cl} values was found to be more consistent.

Thus, with rising values of F_{cl}, we observed three distinct zones of microstructural features and electrical transport behavior in the films. As expected, there is an overlap of microstructural and electrical properties in the transition zones, but, broadly speaking, the F_{cl} values for each of the materials is as follows: type $A = <30\%$, type *C* above 45–50%, and type *B* have values in between the two.

To explain better the classification and our choice of microstructural parameter, we now present the microstructural findings of the three types of films. The microstructural findings of these μc-Si:H samples lay the foundation for the proper understanding of the possible transport mechanisms that govern the different types of electrical transport behaviors observed in the μc-Si:H films having different micro-

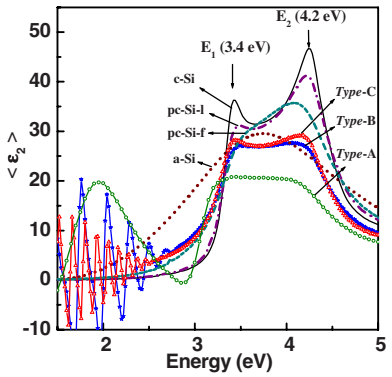

FIG. 1. (Color online) Measured imaginary part of the pseudodielectric function $\langle \varepsilon_2 \rangle$ spectra of samples belonging to different types (A, B, and C). In addition, reference $\langle \varepsilon_2 \rangle$ spectra of c-Si, amorphous silicon, and of low-pressure chemical vapor deposited polysilicon with large (pc-Si-l) and fine (pc-Si-f) grains are shown.

structures. While all the samples of this study have certain general and common microstructural attributes, such as high crystallinity and absence of an amorphous phase, they show many qualitative and quantifiable differences in their morphological and microstructural attributes such as conglomeration, sizes and proportions of different sized crystallite grains, etc. The total crystalline volume fraction in the bulk of all films is more than 90% from the beginning of the growth, with the rest being voids, as revealed by RS and SE analyses. A thin (≈20 nm) film-substrate interface incubation layer is detected by both SE and RS (substrate side), which is less crystalline, having some amorphous content.

We have shown the results of SE studies of the samples in Fig. 1, where we see the measured imaginary part of the pseudodielectric function $\langle \varepsilon_2 \rangle$ spectra of samples belonging to different types (A, B, and C). The optical absorption in c-Si shows two prominent structures, one at ~3.4 eV (E_1) and another at about 4.2 eV (E_2), which are marked in the graph. In contrast, in the dielectric function distribution of a-Si:H, a broad distribution with a maximum around E_1 is present instead. For the interpretation of SE data, we have fitted the experimental data using Bruggeman effective medium approximation (BEMA).[29] We have chosen published dielectric functions for low-pressure chemical vapor deposited polysilicon with large (pc-Si-l) and fine (pc-Si-f) grains as in Ref. 30 in the BEMA model (shown in Fig. 1). In the case of polycrystalline or microcrystalline Si, variations in the peaks of $\langle \varepsilon_2 \rangle$ spectra around the energy positions E_1 and E_2 with crystal size have been both theoretically predicted and experimentally observed.[31,32] In Fig. 1, the broad shoulders in the SE spectrum near 3.4 eV (E_1) and 4.2 eV (E_2) for the types B and C films indicate excellent crystallization with large grains.

For fitting of the experimental SE data, we have used a three layered structure optical model of films that consists of[33]

(i) a bottom layer interfacing with substrate [denoted here as bottom interface layer (BIL)],

(ii) a bulk layer [denoted as middle bulk layer (MBL)] [in the thinner films, due to the lack of dielectric contrast between the bulk layer and the very thin interface layer, we have considered them together as bulk layer (BL)], and

(iii) a top surface roughness layer (denoted here as TSL).

The fractional composition of the films educed from SE data showed crystallite grains of two distinct sizes; the LG is especially evident in the bulk and top surface layers of the films.[18] SE studies of the films at various stages of growth demonstrate the evolution of LG fraction with the film growth, the onset and pattern both being subject to the deposition parameters. We denote the large grain fraction as F_{cl} (mentioned above) and small grain fraction as F_{cf}. Similarly, F_v and F_a denote, respectively, the percentage fractions of voids and amorphous phase. The fractional compositions of the microstructural components present in the different layers (layer thickness d_l) of the three types of μc-Si:H films as deduced from the analyses of SE data are shown in Table I.

We now come to the results of RS measurement carried out on the μc-Si:H samples. The analysis of the RS profiles has been done by a model incorporating the crystallite size distribution (CSD) in the deconvolution procedure.[34,35] In Fig. 2, we have shown the experimental data of RS profiles of the same samples belonging to the three different types, along with the final fitting models. The RS profile of the type-C and type-B μc-Si:H samples evinces a sharp peak at ~520 cm^{-1} corresponding to the transverse optical mode in c-Si, without a signature of the a-Si:H phase (a broad hump around ~480 cm^{-1}), indicating a highly crystalline single-phase material, while such an amorphous hump is present in the RS line of the type-A sample. In contrast, such a hump accompanies the RS profiles from the substrate side of all the samples indicating the presence of an amorphous Si rich material (mixed-phase μc-Si:H) in the glass-film interface region due to the incubation layer.[33] We have used three types of deconvolution models applicable to the RS spectra of all the μc-Si:H samples.[33]

TABLE I. The results of SE data analyses of the samples of types A, B, and C.

SE results	Type A		Type B			Type C		
	TSL	BL	TSL	MBL	BIL	TSL	MBL	BIL
d_l (nm)	7.9	48.2	4.2	423.6	21.7	4.3	986.2	32.6
F_{cf} (%)	67.1	88.4	43	58.7	0	15	30.5	79.5
F_{cl} (%)	0.6	0	32	37.6	0	59	67	0
F_a (%)	0	1.5	0	0	90.6	0	0	0
F_v (%)	32.3	10.1	25	3.7	9.4	26	2.6	20.5

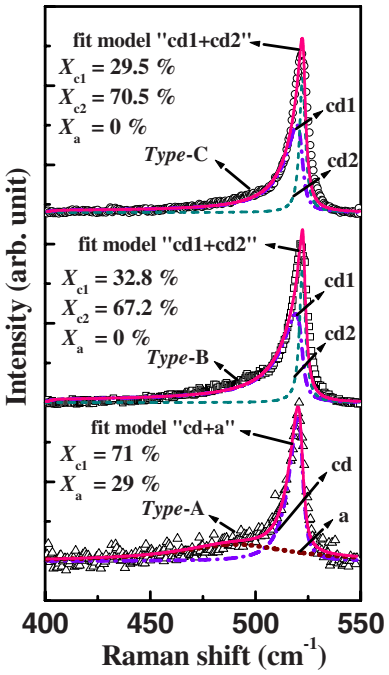

FIG. 2. (Color online) Deconvolution results consisting of the total fit and the deconvoluted peaks for the RS profiles of samples of three types: *A*, *B*, and *C*.

(1) Model: cd1+cd2+*a*—incorporating a bimodal CSD [small (cd1) and large (cd2) crystallites] along with an amorphous phase.

(2) Model: cd1+cd2—incorporating a bimodal CSD without an amorphous background.

(3) Model: cd+*a*—incorporating a unimodal CSD (mainly the contribution from small sized crystallites) with an amorphous background.

The percentage volume fractions of large and small crystallites (X_{c1} and X_{c2}, respectively) and that of amorphous content (X_a) as deduced from RS analyses are mentioned in Fig. 2, for each type of material. There is a significant variation in the percentage fraction of the constituent LG and SG with film growth, as demonstrated by the RS and SE studies carried out on the films at various stages of growth.[18,33] The percentage volume fractions of constituent grains and phases are more accurately determined by SE due to its capability to recognize the individual layers on the basis of the contrast between their dielectric properties.[33] Since the microstructural data of the bulk layer are more important for coplanar electrical transport measurements, the F_{cl} values of the bulk layer were used in analyzing the correlation of microstructure to the electrical transport behavior.

The XRD results have demonstrated the presence of two different sized crystallites. Preferential orientation in (400) and (220) directions was achieved by optimizing the deposition conditions leading to smooth top surfaces (surface roughness <3 nm). The evolution of the conglomeration of crystallites under different deposition conditions was demonstrated by AFM results.[18] The AFM images of three representative samples of each type are shown in Fig. 3, where we get a visual idea about the morphology of the films. In the type-*A* film, most of the surface (~90%) is covered with

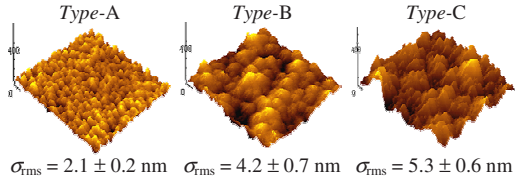

FIG. 3. (Color online) Three dimensional AFM images (1000 × 1000 nm^2) of the same films (as shown in Figs. 1 and 2) of three types: *A*, *B*, and *C*. The root mean square (rms) values of surface roughness (σ_{rms}) are mentioned in each image.

surface grains of the size ~35–50 nm evolving out of the surface. These surface grains are closely packed, but a clear boundary region isolates them from each other. No conglomeration of grains is seen. In the type-*B* film, the average size of the surface grains are 75–90 nm; however, few of them conglomerate to form surface grains of the size of 150–175 nm. Finally, in the type-*C* film, a significant amount of conglomeration is seen with the spherical shaped conglomerate surface grains measuring up to 325–350 nm. The constituents of these large surface conglomerate grains are of the size of 70–80 nm.

Considering all the microstructural findings and correlating with the type of electrical transport behavior observed in each range of F_{cl} values, we now present the classification in Fig. 4, where the variation of σ_0 and E_a of the three types of films with F_{cl} is shown. To summarize this classification, the type-*A* films have small grains, low amount of conglomeration (without column formation), and high density of intergrain boundary regions containing disordered phase. In this type, $F_{cl}<30\%$, σ_0 and E_a are constant [$\approx 10^3$ $(\Omega\ \mathrm{cm})^{-1}$ and ≈ 0.55 eV, respectively]. The type-*B* films contain a fixed ratio of mixed grains in the bulk. There is a marked morphological variation in these films due to the commencement of the conglomeration of grains resulting in column formation, and a moderate amount of disordered phase is present in the columnar boundaries. Here, F_{cl} varies from 30% to 45%, and there is a sharp drop in σ_0 [from $\approx 10^3$ to 0.1 $(\Omega\ \mathrm{cm})^{-1}$] and E_a (from ≈ 0.55 to 0.2 eV). The type-*C* μc-Si:H material is fully crystalline, crystallite conglomerates are densely packed with a significant fraction of large crystallites (>50%), and a preferential orientation is seen. Here, σ_0 shows a rising trend [from 0.05 to 1 $(\Omega\ \mathrm{cm})^{-1}$] and the fall in E_a is slowed down (from 0.2 to 0.10 eV). The microstructural features that result in such changes in the electrical transport behavior are discussed later.

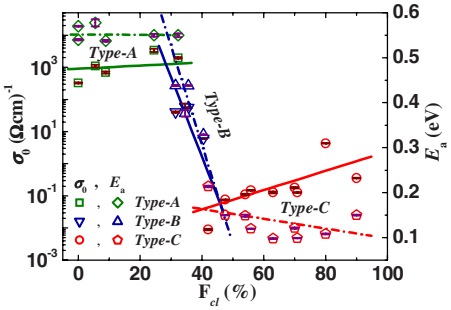

FIG. 4. (Color online) Variation of σ_0 and E_a of μc-Si:H samples (types *A*, *B*, and *C*) with F_{cl}.

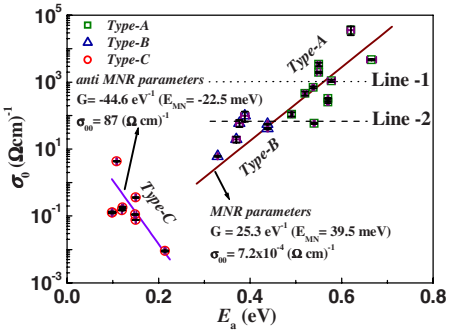

FIG. 5. (Color online) Correlation between σ_0 and E_a in *undoped* μc-Si:H samples (types *A*, *B*, and *C*). The samples of types *A* and *B* follow MNR while the type-*C* material shows anti-MNR behavior with parameters as shown in the graph. In the MNR region, the dotted line (line 1) indicates the possible position of σ_0 where $\gamma_F \approx 0$ and the dashed line (line 2) where $\gamma_F \approx \gamma_C$.

While a relation between the F_{cl} and electrical transport parameters is evident in Fig. 4, it is also observed that there is some relation between σ_0 and E_a. Therefore, it would be useful to study the variation of σ_0 with E_a for each type of material. Figure 5 shows a semilogarithmic plot between σ_0 and the E_a obtained on our samples. The data for types *A* and *B* are found to fall along the MNR line. We found the values of the MNR parameters, $G \approx 25.3$ eV^{-1} (or $E_{\mathrm{MN}} \approx 39.5$ meV) and $\sigma_{00} \approx 7.2 \times 10^{-4}$ $(\Omega\,\mathrm{cm})^{-1}$ from the fit shown in the figure. In contrast, the data for samples of type *C* show an inverse linear relationship between the logarithmic values of σ_0 and E_a. The correlation between σ_0 and E_a appears to change sign in this case, demonstrating *anti-MNR* and the values of the MNR parameters are $G \approx -4.6$ eV^{-1} or $E_{\mathrm{MN}} \approx -22.5$ meV and $\sigma_0 \approx 86.8$ $(\Omega\,\mathrm{cm})^{-1}$.

IV. DISCUSSION

In order to understand the MNR parameters, anti-MNR phenomenon, and their significance, we discuss here the applicability of the existing statistical shift model developed for *a*-Si:H in explaining both MNR and anti-MNR behaviors in the conductivity of μc-Si:H. In a disordered semiconductor, the DOS distribution may not be symmetrical with respect to the band center due to tailing of localized states at the band edges as well as defect states in the gap. Therefore, the position of E_F is determined by the shape of the DOS, i.e., at $T=0$ K, E_F may be at some position other than the midgap. However, as the temperature increases, electrons and holes are thermally excited to states at the band edges, and charge neutrality condition requires a statistical shift of E_F toward midgap. Therefore, the experimentally obtained σ_0 contains terms arising from the two effects. The first comes from the statistical shift of E_F, and the second involves a temperature dependent shift of the band edges, i.e., of conduction and valence band edges, E_c and E_v.[4] According to Mott, one can express the conductivity expression as[36]

$$\sigma_d(T) = \sigma_M \exp[-(E_c - E_F)/kT], \tag{3}$$

where σ_M is minimum metallic conductivity. E_c and E_F are both dependent on temperature. Approximating the temperature shift of E_c and E_F to be linear functions with the slopes γ_c and γ_F, respectively, we get

$$E_c(T) = E_c^0 - \gamma_c T \quad \text{and} \quad E_F(T) = E_F^0 - \gamma_F T, \tag{4}$$

where E_c^0 and E_F^0 are the positions of E_c and E_F at $T=0$ K. After inserting Eq. (4) into Eq. (3), we get Eq. (2) with

$$E_a = E_c^0 - E_F^0, \tag{5}$$

$$\sigma_0 = \sigma_M \exp[(\gamma_c - \gamma_F)/k]. \tag{6}$$

The band shifts are taken relative to the midgap. They are positive when E_c and E_F move toward the midgap.

Normal MNR in μc-Si:H has been generally understood using the above calculations, but the anti-MNR behavior is rather less elucidated. Most workers[22,23] have attributed the anti-MNR behavior observed in the doped μc-Si:H material to the model implicating the energy band diagram of crystalline silicon (*c*-Si) and *a*-Si:H interfaces, as proposed by Lucovsky and Overhof.[20] According to this model, anti-MNR can be observed only in a degenerate case when very heavy doping of the μc-Si:H material causes E_F to move above E_c in the crystalline phase; consequently, E_F can move deeply into the tail states in the disordered region. In explaining the anti-MNR behavior on the basis of this energy band diagram, equal band edge discontinuities at both ends of *c*-Si and *a*-Si:H interfaces were assumed.[20] A similar argument was also given by Meiling and Schropp[23] in their study of intrinsic het-Si TFT. But it is not a clear-cut task to calculate the energy band diagram of the interface because the band edge discontinuities are not really well established, as some studies have claimed the band edge discontinuities between crystalline grains and amorphous tissue regions to be most pronounced in the conduction band (CB),[37] while others have attributed the discontinuity mainly to the valence band.[38,39] However, recent findings support the latter contention.[40]

The loss of linearity of the relationship between E_a and log σ_0 (i.e., anti-MNR) in *a*-Si:H has been observed for both very high and very low values of E_a in theoretical studies where calculations based on the statistical shift model were applied.[5–9] In these studies, the occurrence of anti-MNR at high E_a in *a*-Si:H has been dealt with by employing both experimental and theoretical approaches. However, the lack of experimental evidence for anti-MNR at low E_a in *a*-Si:H was probably the reason why it was not elaborated theoretically in much detail.[41] An important insight these studies offer is that the occurrence of anti-MNR depends on the DOS distributions and the position of the E_F in the *a*-Si:H material. These studies are relevant for μc-Si:H because the same conditions that give rise to anti-MNR in *a*-Si:H at low E_a may be applicable in the μc-Si:H system as well. The linear relation between log σ_0 and E_a in *a*-Si:H is obtained only if E_F lies in the CB tail or close to the minimum of DOS. However, there may exist a combination of factors, which can serve to either augment or diminish the anti-MNR effect. For instance, when E_F approaches the boundaries, if there is a flat DOS spectrum near the edge, the statistical shift of E_F will diminish along with a decrease in the temperature derivative of E_F. This causes anti-MNR behavior for small and large E_a regions.[8,9] However, such a deviation

(anti-MNR effect) may diminish if there is a jump in the DOS profile present at the edge of the steep tail.[9] Another situation is where the anti-MNR is more pronounced at values of E_a on the lower side when the DOS value at the minimum reduces.[9] Such a reduction in DOS value at the minimum, where exponential CB and negatively charged dangling bond (DB^-) tails meet, has been observed in the case of *n*-type doping of *a*-Si:H.[42–44] Here, DOS of the DB^- band increases with increased doping level. The failure of MNR at the higher E_a side can be seen when E_F lies far in the tail of the DB^- states or in intrinsic materials where DOS at the midgap is almost flat due to which the temperature derivative of E_F will be very little or almost zero.[9]

An important aspect of understanding electronic transport is the actual conduction route. All the above concepts hold true for μc-Si:H only if a band tail transport exists. There has been a lack of consensus on what the current flow pathway is in fully crystalline undoped μc-Si:H. One school of thought propounds the idea that conduction takes place through individual crystallites or aggregates thereof (columns).[45,46] In discussing transport mechanisms in μc-Si:H, we need to distinguish between highly doped samples and undoped or unintentionally doped samples. In the heavily doped μc-Si:H material, current route follows through crystallites/columns, and transport properties can be understood by well established grain boundary trapping models. However, an alternate viewpoint that is also borne out by recent experimental evidence suggests a dominant role of the disordered silicon tissue of the boundaries encapsulating the crystallite columns in electrical transport in fully crystalline single-phase undoped μc-Si:H material.[19]

Therefore, in order to understand the transport data of our μc-Si:H samples, we need to consider the data not only in the context of the respective sample microstructures, but also with respect to the above-discussed theoretical background and the possible current routes in the material. Though many studies have reported on electrical transport properties of highly crystalline μc-Si:H materials, it is noteworthy that in these cases, such high crystallinity ($>80\%$) is achieved around the time when column formation is also complete during the film growth process.[47,48] In the poorly crystalline μc-Si:H material, where an interconnected network of boundary tissue has not formed, transport is considered to take place through the amorphous matrix.[19] Our material is somewhat different, as it achieves full crystallization from the beginning of the growth due to the use of SiF_4 in deposition, which is especially relevant in the type-*A* material, where there is almost complete crystallization, without an amorphous matrix, though the column formation has not started.[18,27] The type-*A* material consists mainly of SG with an increased number of SG boundaries. Therefore, the question of formation of potential barrier (i.e., transport through crystallites) does not arise because the large number of defect and/or trap sites compared to free electrons and small size of crystallites will result in a depletion width that is sufficiently large to become greater than the grain size, causing the entire grain to be depleted.[45] As a result, the transport will be governed by the band tail transport. Corroboratively, a look at Fig. 4 shows that in the type-*A* material, E_a becomes nearly saturated ($\approx$0.55 eV) and σ_0 reaches $\approx 10^3$ $(\Omega\,\mathrm{cm})^{-1}$. This means that the E_F is lying in the gap where the DOS does not vary much and there is a minimal movement of E_F, or $\gamma_F \approx 0$.[6–8] We have indicated this possible position of σ_0, where $\gamma_F=0$ in Fig. 5 by a dotted line (line 1). The initial data points shown in Fig. 5 for type *A* have higher σ_0 [$\approx 10^4$ $(\Omega\,\mathrm{cm})^{-1}$] and E_a ($\approx$0.66 eV) because of a shift in E_c and/or a negative value of γ_F, as what happens in *a*-Si:H for E_a toward the higher side.[6–8]

In the type-*B* material, many morphological changes occur during the film growth, column formation has commenced, and there is a change in the transport routes. It is a crossover region from type *A* to type *C* that shows large variations in σ_0 and its E_a, as seen in Fig. 4. The improvement in film microstructure leads to a delocalization of the tail states causing the E_F to move toward the band edges, closer to the current path at E_c. The statistical shift γ_F depends on the temperature and the initial position of E_F, and when the E_F is closer to any of the tail states and the tail states are steep, γ_F is rapid and marked. In fact, any μc-Si:H material with such microstructural attributes as in the type-B material, will show a rapid change in γ_F. In Fig. 5, the transition between type-*A* and type-*B* materials shows a few data points somewhat scattered around the MNR line, belonging to both types, which show a more or less constant σ_0 [70–90 $(\Omega\,\mathrm{cm})^{-1}$] with the fall in E_a (0.54–0.40 eV), indicating that the temperature shift of E_F and that of the CB have become equal, canceling each other out (i.e., $\gamma_F \approx \gamma_c$).[6–8] We have depicted the possible position of σ_0, where such a situation can occur in Fig. 2 by a dashed line (line-2). In this case, the E_F is pinned near the minimum of the DOS between the exponential CB tail and the tail of the defect states (DB^-).[6–8] With increasing crystallinity and/or improvement in the microstructure, the minimum shifts toward E_c, leading to a decrease of E_a.

In the type-*C* material, one can erroneously assume the apparent low values of E_a to be a GB barrier height formed at the interface between neighboring crystallites/columns, and the appearance of reduction in E_a to be a reduction in barrier height with film growth and/or increasing F_{cl} (as shown in Fig. 4), in a manner similar to the situation when the mobility-barrier height variation is seen to match the conductivity E_a with increase in doping.[49] The calculated values of free electron concentrations (from μ_{TRMC}, σ_d, and E_a data) do not suggest the possibility of unintentional doping achieving such a high value of background doping concentration. So, the unintentional doping resulting in degeneracy is not possible either. Therefore, the energy band model as suggested by Lucovsky and Overhof seems inapplicable to our undoped μc-Si:H case, though the value of E_{MN} here is close to the value reported in heavily doped μc-Si:H (−20 meV).[20] Also, in a degenerate case, the conductivity behavior of polycrystalline material is found to exhibit a T^2 dependence of σ_d,[50] which is not so in our material. In type-*C* μc-Si:H material, a higher F_{cl} and large size of columns ($>$300 nm) result in less columnar boundaries and, therefore, less defects associated with the boundaries. In addition, a well-established conducting network of such interconnected boundaries is formed in this material, which results in higher conductivity (rise in σ_0). Considering transport

through the encapsulating disordered tissue, a band tail transport is mandatory. The large columnar microstructure results in a long range ordering, which is sufficient to delocalize an appreciable range of states in the tail state distribution. In addition, higher density of available free carriers and low value of defect density can cause a large increase in DB^- density together with a decrease in positively charged dangling bond (DB^+) states in the gap, which results in a lower DOS near the CB edge and can create a possibility of a steeper CB tail. In this situation, if E_F lies in the plateau region of the DOS, it may create an anti-MNR situation.

Our experimental and modeling study of phototransport properties of these three types of μc-Si:H materials had evinced a fundamental change taking place in the DOS distributions along with change in microstructure and electrical transport properties.[51–53] Therefore, as we go from one type of material to another, a change occurs in the DOS of the transport path elements as well, and this DOS cannot be assumed to be similar to that of either *a*-Si:H or *c*-Si because the unique film microstructure will have an effect on it. Our proposed effective DOS distributions are different for the three types of μc-Si:H materials and exhibit structured band tails: a sharper, shallow tail originating from grain boundary defects and another less steeper deep tail associated with the defects in the columnar boundary regions, both of which have an exponential distribution.[51–53] Therefore, considering all the above reasons, a band tail transport presents an experimentally and theoretically consistent picture of the transport in our μc-Si:H materials.

Anti-MNR behavior in undoped μc-Si:H has not been explicitly reported in literature, to the knowledge of the authors. When we suggest that the anti-MNR behavior observed in our type-*C* material has not anomalously arisen from unintentional doping (which has been ruled out in discussions above), and is explainable solely on the basis of DOS features, it follows naturally that similar reproducible anti-MNR relationships should be found in similar types of undoped μc-Si:H materials. With this aim, we have analyzed the transport data of highly crystalline undoped μc-Si:H materials reported in literature to see whether we can find any signature of anti-MNR in those data. Many of these works were not concerned with the study of conductivity behavior in the context of MNR or anti-MNR, and where the relevant parameter values were not given explicitly, we have determined them by analyzing the data published in these papers for the presence of MNR and anti-MNR in their materials. Figure 6(a) shows the plot between σ_0 and E_a of undoped μc-Si:H material (case 1) and *p*-doped μc-Si:H material (case 2), the values of which have been derived from data in literature. Also shown in this figure are the reported results on *a*-Si:H (typical MNR, case 3, Ref. 54). For the purpose of comparability, our data (types *A*, *B*, and *C* μc-Si:H materials) are shown by the solid line, which is the same fitted line shown in Fig. 5. Figure 6(b) (cases 4 and 5) shows the plot between σ_0 and E_a for the doped μc-Si:H material reported in literature. The reported results of MNR and anti-MNR in doped μc-Si:H from Flückiger *et al.* (case 6) and those of anti-MNR in heavily doped μc-Si:H from Lucovsky and Overhof[20] (case 7) are also shown in Fig. 6(b). Though MNR and anti MNR behaviors are visible on even a cursory look at the figures, we will now take up each data and examine it in relation to the sample microstructure, as reported in the respective paper. The various data that fall in the MNR region show a variation in the MNR parameters *G* and σ_{00}, the values of which are mentioned in the figure captions. *G* is a strong function of the DOS in the mobility gap and thus of the position of E_F. It varies from one DOS to another and if the slope of DOS around the minima becomes steeper, *G* increases.

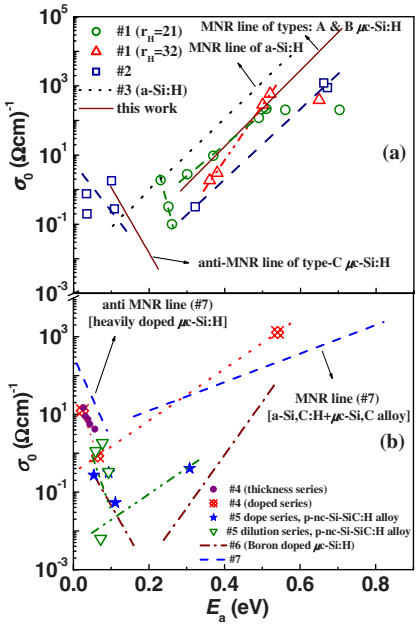

FIG. 6. (Color online) Plot of σ_0 as a function of E_a for data of heavily doped, doped, and undoped μc-Si:H, *p*-nc-Si-SiC:H alloy, *a*-Si,C:H+μc-Si,C alloy, and *a*-Si:H obtained from literature. (a) Case 1 (Ref. 47), case 2 (Ref. 55), and case 3 (Ref. 54). (b) Similar data for case 4 (Ref. 56), case 5 (Refs. 58 and 59), case 6 (Ref. 21), and case 7 (Ref. 20). The solid line represents our data.

First, we take up case 1 [Fig. 6(a), data of Kočka *et al.*[47]]. Here, the samples deposited at r_H (H_2/SiH_4)=21 (4.5% dilution) have thicknesses of 0.07–4.7 μm and those at r_H =32 (3% dilution) have thicknesses of 0.1 to 1.7 μm. The electrical transport data of these samples show MNR behavior, and the *G* of these two series of samples of r_H=21 and 32 are 20 and 36 eV^{-1}, respectively, which signifies that the CBT should be steeper for the latter case. The samples of r_H=21 series that are thicker than 1 μm show anti-MNR; here, the crystallinity has reached a constant value of ≈90%, and the material has a densely packed columnar microstructure.

The second data of Collins *et al.*[55] [Fig. 6(a), case 2] incorporate the data of *p*-doped μc-Si:H material having a fixed and low amount of doping, but it is the H_2 dilution and not doping level that is altered to yield different microstructures in this study. Therefore, these data have not been included with the doped sample data shown in Fig. 6(b). The samples of this case belong to three types of materials, namely, amorphous films of low conductivity and high E_a (0.67 eV) obtained with *R* (=H_2/SiH_4) <80, mixed-phase (a+μc)-Si:H films (E_a falls with rise in *R*, and σ_d increases)

obtained with $80<R<160$, and single-phase μc-Si:H films (E_a is very low, $\approx$0.1 eV) obtained with $R>160$ in which nucleation of microcrystallites occurs immediately on the ZnO substrate without an amorphous interlayer. The first two types of materials show an MNR behavior, while the data of the material described as single-phase μc-Si:H exhibits an anti-MNR behavior.

In case 4 [Fig. 6(b), He *et al.*[56]], the data consist of two series. The first series consists of doped samples (starting with an undoped sample and progressively increasing the doping level) having a constant thickness. The second series consists of doped samples with systematically reduced thicknesses, but fixed doping. In the first series, as we proceed from the undoped sample to the sample with the highest doping, a change from MNR to anti-MNR behavior is seen. However, in the second series, as the thickness is reduced, σ_0 falls with an increase in E_a, still following the anti-MNR line, demonstrating that with microstructural changes, the anti-MNR effect reduces. The G value is $\approx$15.6 eV^{-1}, which means that the slope of CBT is larger than that of our materials. This might be because in heavily doped case, doping may systematically increase the extent of the tail states since in n-type doping the dominant charged defects are P_4^+ and DB^- and the rate of increase of the P_4^+ defect density is faster than that of DB^-.[57] It is evident from cases 2 and 4 that the anti-MNR behavior is not just an effect of doping but is an outcome of fundamental microstructural attributes.

Now, we consider case 5 [Fig. 6(b), Myong *et al.*[58,59]], which shows the data of hydrogenated boron (B)-doped nc-Si-SiC:H (p-nc-Si-SiC:H alloy) material. This is similar to the μc-Si,C alloy material mentioned in Ref. 20, in which the possibility of anti-MNR induced by doping was ruled out. The reason stated for this was that it is improbable that the Si crystallites can be doped to such a degree that the E_F is driven deep into the band-tail state distribution of the a-Si,C:H phase. The material in case 5 contains nc-Si grains embedded in the a-SiC:H matrix. We have analyzed the data of two types of samples of this material. In the first type of samples (doping series),[58] boron doping was increased while H_2 dilution was kept constant at 20. The second series (dilution series)[59] consists of samples deposited under constant boron doping ($B_2H_6/SiH_4=1000$ ppm) and varying H_2 dilution ($H_2/SiH_4=15-30$). The film thickness is constant in both the series. In the doping series, σ_d is reported to follow MNR with a very high value of E_{MN} ($\approx$295 meV), which has been explained by thermally activated hopping between neighboring crystallites dominating the carrier transport in the $T>150$ K regime.[58] The possibility of extended-state transport was ruled out in the study.[58] The dilution series has not been studied for MNR behavior in this work.[59] When we plot together the data of samples of both the series, the result surprisingly reveals evidence of anti-MNR behavior in addition to MNR behavior [see Fig. 6(b)]. The only sample with data lying in the MNR region is a completely amorphous highly doped ($B_2H_6/SiH_4=8000$ ppm) material with 0% crystallinity. Another sample ($B_2H_6/SiH_4=8000$ ppm and crystalline volume fraction=22.8%) lies in the intermediate region, while the rest of the samples have values well within the anti-MNR region, and it is the transition region between these two extremes which has been reported in Ref. 58. When E_{MN} is recalculated from this MNR line (after neglecting the anti-MNR data), the value of E_{MN} is $\approx$65 meV, which is closer to the typical E_{MN} values reported for MNR line in a-Si:H or μc-Si:H materials. This suggests that an anti-MNR behavior is possible in this kind of nc-Si-SiC:H alloy material also, which has not been reported previously and certainly needs more exploration. It seems likely that the transport mechanism in the MNR regime in this material is not thermally activated hopping[54] as suggested in Ref. 58. Both the MNR and the anti-MNR behavior in this nc-Si-SiC:H alloy material can be better understood by the same statistical shift model that we have used to explain MNR and anti-MNR behaviors observed in our material.

Case 6 [Fig. 6(b), Flückiger *et al.*[21]] consists of the data of a highly crystalline μc-Si:H material studied for compensation doping (p-type doping with boron) that shows a transition from anti-MNR to MNR behavior with increasing doping. The initial point of anti-MNR therefore belongs to the undoped material, and the deposition technique used there (very high-frequency-glow discharge) results in a high crystallinity and such microstructural attributes that can result in the anti-MNR behavior.

All the above data suggest that anti-MNR is possible in undoped μc-Si:H materials. Anti-MNR has been reported in TFTs incorporating intrinsic heterogeneous Si, but it was explained by applying the Lucovsky and Overhof model.[23] The material in this particular report consisted of cone shaped Si crystals embedded in an amorphous matrix (the cones initiate at the SiO_2 surface), and the samples showing anti-MNR had fully coalescent crystallites growing perpendicular to the substrate surface, quite similar to our type-C material where anti-MNR is seen. In the view of all the evidence from our study, it seems possible that the statistical shift model can explain the anti-MNR in het-Si as well. The MNR and anti-MNR parameters for all the above-discussed cases are given in Table II.

All the above discussions demonstrate that MNR is valid for the whole class of μc-Si:H materials. The value of MNR parameter G for a particular μc-Si:H material is related to the microstructure and DOS characteristic of that material, although different sets of MNR parameters G and σ_{00} values can exist for the materials of the same μc-Si:H system. We have tried to explain the variation and significance of G in the above discussions. Now, it would be desirable to explore the variation in the values of σ_{00} as well and understand what σ_{00} really means in the context of the material. All the above data, including those of ours, have provided us with a number of G and σ_{00} values, which should be useful to get an insight into a relationship between the two, similar to the relationship derived by Drusedau *et al.*[6,7] If we compare Eqs. (1) and (6), we find a relationship between the MNR parameter σ_{00} and the fundamental preexponential factor or minimum metallic conductivity σ_M as

$$\sigma_{00} = \sigma_M \exp[(\gamma_c - \gamma_F)/k - GE_a]. \quad (7)$$

Applying Eq. (5), we get

$$\sigma_{00} = \sigma_M \exp[(\gamma_c - \gamma_F)/k - G(E_c^0 - E_F^0)]. \quad (8)$$

TABLE II. List of MNR and anti-MNR parameters for all the cases studied.

	MNR parameters			Anti-MNR parameters		
Samples	σ_{00} $(\Omega\ \mathrm{cm})^{-1}$	G (eV^{-1})	E_{MN} (meV)	σ_{00} $(\Omega\ \mathrm{cm})^{-1}$	G (eV^{-1})	E_{MN} (meV)
This work						
Types *A* and *B*	7.2×10^{-4}	25.3	39.5			
Type *C*				87	−44.6	−22.5
Published Data						
Case 1 (r_{H}=21)	4×10^{-3}	20.7	48.4	1.26×10^{10}	−97.7	−10.2
Case 1 (r_{H}=32)	3.2×10^{-6}	36.6	27.3			
Case 2	1.7×10^{-4}	23.4	42.7	6	−32.5	−30.8
Case 3	7.7×10^{-3}	24	41.6			
Case 4	0.32	15.4	65.1	59	−66.1	−15.1
Case 5	4.2×10^{-3}	15.3	65.4	21	−64.9	−15.4
Case 6	3.2×10^{-6}	31.3	31.9	2.4	−39.9	−25.1
Case 7	2.3	8.5	118.3	309	−49.5	−20.2
Case 8	0.5	11.8	84.5			
Case 9	7.2×10^{-3}	20	50			

For a set of samples such as in our case where μc-Si:H materials possess different DOSs, the average statistical shifts of E_F can be assumed to be identical with the temperature coefficient γ_F of E_F and can be represented as a function of the position of E_F with an energy $(E_c^0-E_{\mathrm{min}})$ at which there is effectively no shift, i.e., $\gamma_F\ (E_c^0-E_{\mathrm{min}})=0$. Then, the above equation reduces to

$$\sigma_{00}=\sigma_M \exp[(\gamma_c/k-GE_{\mathrm{min}})]. \tag{9}$$

If the shift in band edges γ_c is known, then for such a value of σ_{00} where $G=0$ (derived by extrapolation), one can obtain the value of σ_M. This information can further provide those values of σ_0 [from Eq. (6)], where $\gamma_F=0$ and where $\gamma_c=\gamma_F$, both very important positions for providing simplified information about the nature of carrier transport in the material. The quantity E_{min} is a measure for the position of the DOS minimum within the mobility gap. In Fig. 7, we have plotted G with σ_{00} derived from the data of the above groups [shown in Figs. 6(a) and 6(b)] and other groups from literature [case 8 (Ref. 60) and case 9 (Ref. 54)]. The solid line shows the fit using Eq. (9). From here, we have calculated the value of σ_M (where $\gamma_F=\gamma_c$) $\approx100\ (\Omega\ \mathrm{cm})^{-1}$ and found the minimum value of $E_{\mathrm{min}}\approx0.61$ eV, which is a measure of the position of the DOS minimum within the gap. Using these values, we find $\sigma_0\approx1.2\times10^3\ (\Omega\ \mathrm{cm})^{-1}$ when $\gamma_F=0$. Consolidating all these data and comparing with the analysis of the data in Fig. 5 (Line-1 and Line-2), we find that our data are corroborative with these values that have been derived for a large number and variety of μc-Si:H materials, representative of the generic μc-Si:H system.

It follows from this study that a shift in the Fermi level of μc-Si:H materials induced by any means (doping or any change in microstructure and the consequent DOS features) can give rise to an appearance of MNR behavior in the dc conductivity. Thus, the application of the statistical shift model to the experimentally observed MNR parameters leads us to the information about some fundamental carrier transport parameters of the μc-Si:H material and a knowledge about the physical basis of MNR behavior, all with considerable simplicity.

V. CONCLUSION

In conclusion, both MNR and anti-MNR can be seen in the dark conductivity behavior of highly crystalline single-phase undoped μc-Si:H material, depending on the microstructure and the correlative DOS features. We have shown the applicability of the percentage fraction of constituent

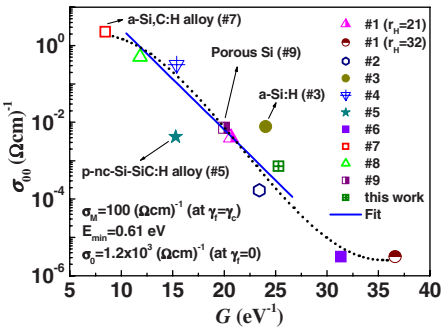

FIG. 7. (Color online) Relationship between σ_{00} and G for cases 1–7 of Fig. 3, case 8 (Ref. 60), case 9 (Ref. 54), and our data. The solid line shows the fit.

crystalline grains in fully crystalline μc-Si:H materials in predicting electrical transport behavior. The transport mechanism in μc-Si:H has largely been a moot point in literature. Our study strongly indicates the presence of a band tail transport in μc-Si:H. We have shown that the statistical shift model can successfully explain both MNR and anti-MNR behaviors in our material. Our assertions are further validated by the analysis of experimental μc-Si:H transport data available in literature. We have derived well-substantiated and generalized values of $E_{\min}$, σ_M, and values of σ_0 and E_a where $\gamma_F=0$ and $\gamma_F=\gamma_c$, which hold true for the μc-Si:H system as a whole and can further add to our understanding of the electrical transport in this heterogeneous material.

*Corresponding author: skram@iitk.ac.in and sanjayk.ram@gmail.com
†satyen@iitk.ac.in

[1] W. Meyer and H. Neldel, Z. Tech. Phys. (Leipzig) **18**, 588 (1937).
[2] W. B. Jackson, Phys. Rev. B **38**, 3595 (1988).
[3] A. Yelon, B. Movaghar, and H. M. Branz, Phys. Rev. B **46**, 12244 (1992).
[4] H. Overhof and W. Beyer, Philos. Mag. B **47**, 377 (1983).
[5] B. G. Yoon, C. Lee, and J. Jang, J. Appl. Phys. **60**, 673 (1986).
[6] T. Drusedau and R. Bindemann, Phys. Status Solidi B **136**, K61 (1986).
[7] T. Drusedau, D. Wegener, and R. Bindemann, Phys. Status Solidi B **140**, K27 (1987).
[8] J. Stuke, J. Non-Cryst. Solids **97-98**, 1 (1987).
[9] Minoru Kikuchi, J. Appl. Phys. **64**, 4997 (1988).
[10] S. R. Elliott, *Physics of Amorphous Materials*, 2nd ed. (Longman Group UK Limited, England, 1990).
[11] E. Vallat-Sauvain, U. Kroll, J. Meier, N. Wyrsch, and A. Shah, J. Non-Cryst. Solids **266-269**, 125 (2000).
[12] M. Luysberg, P. Hapke, R. Carius, and F. Finger, Philos. Mag. A **75**, 31 (1997).
[13] L. Houben, M. Luysberg, P. Hapke, R. Carius, F. Finger, and H. Wagner, Philos. Mag. A **77**, 1447 (1998).
[14] G. Lucovsky, C. Wang, M. J. Williams, Y. L. Chen, and D. M. Maher, Mater. Res. Soc. Symp. Proc. **283**, 443 (1993).
[15] R. Vanderhaghen, S. Kasouit, J. Damon Lacoste, F. Linu, and P. Roca i Cabarrocas, J. Non-Cryst. Solids **338-340**, 336 (2004).
[16] S. Kumar, R. Brenot, B. Kalache, V. Tripathi, R. Vanderhaghen, B. Drevillon, and P. Roca i Cabarrocas, Solid State Phenom. **80-81**, 237 (2001).
[17] P. Roca i Cabarrocas, S. Kasouit, B. Kalache, R. Vanderhaghen, Y. Bonnassieux, M. Elyaakoubi, and I. French, Inf. Disp. **12**, 1 (2004), and references therein.
[18] S. K. Ram, D. Deva, P. Roca i Cabarrocas, and S. Kumar, Thin Solid Films **515**, 7619 (2007).
[19] D. Azulay, I. Balberg, V. Chu, J. P. Conde, and O. Millo, Phys. Rev. B **71**, 113304 (2005), and references therein.
[20] G. Lucovsky and H. Overhof, J. Non-Cryst. Solids **164-166**, 973 (1993).
[21] R. Flückiger, J. Meier, M. Goetz, and A. Shah, J. Appl. Phys. **77**, 712 (1995).
[22] R. Brüggemann, M. Rojahn, and M. Rösch, Phys. Status Solidi A **166**, R11 (1998).
[23] H. Meiling and R. E. I. Schropp, Appl. Phys. Lett. **74**, 1012 (1999).
[24] M. Goerlitzer, N. Beck, P. Torres, U. Kroll, H. Keppner, J. Meier, J. Koehler, N. Wyrsch, and A. Shah, Mater. Res. Soc. Symp. Proc. **467**, 301 (1997).
[25] B. Yan, G. Yue, J. M. Owens, J. Yang, and S. Guha, Appl. Phys. Lett. **85**, 1925 (2004).
[26] C. H. Lee, A. Sazonov, A. Nathan, and J. Robertson, Appl. Phys. Lett. **89**, 252101 (2006).
[27] S. K. Ram, Ph.D. thesis, I.I.T. Kanpur, India, 2006.
[28] S. K. Ram, P. Roca i Cabarrocas, and S. Kumar, Thin Solid Films **515**, 7469 (2007).
[29] D. A. G. Bruggeman, Ann. Phys. **24**, 636 (1935).
[30] G. E. Jellison, Jr., M. F. Chisholm, and S. M. Gorbatkin, Appl. Phys. Lett. **62**, 3348 (1993).
[31] S. Kumar, B. Drevillon, and C. Godet, J. Appl. Phys. **60**, 1542 (1986).
[32] B. Drevillon, Prog. Cryst. Growth Charact. Mater. **27**, 1 (1993).
[33] S. K. Ram, Md. N. Islam, S. Kumar, and P. Roca i Cabarrocas, Thin Solid Films, doi:10.1016/j.tsf.2007.12.113 (2008).
[34] Md. N. Islam and S. Kumar, Appl. Phys. Lett. **78**, 715 (2001).
[35] Md. N. Islam, A. Pradhan, and S. Kumar, J. Appl. Phys. **98**, 024309 (2005).
[36] N. F. Mott and E. A. Davis, *Electronic Processes in Non-Crystalline Materials*, 2nd ed. (Oxford University Press, New York, 1979).
[37] M. Cuniot and Y. Marfaing, Philos. Mag. B **57**, 291 (1988).
[38] H. Mimura and Y. Hatanaka, Appl. Phys. Lett. **50**, 326 (1987).
[39] X. Xu, J. Yang, A. Banerjee, S. Guha, K. Vasanth, and S. Wagner, Appl. Phys. Lett. **67**, 2323 (1995).
[40] S. Hamma and P. Roca i Cabarrocas, Appl. Phys. Lett. **74**, 3218 (1999).
[41] P. Irsigler, D. Wagner, and D. J. Dunstan, J. Phys. C **16**, 6605 (1983).
[42] M. J. Powell and S. C. Deane, Phys. Rev. B **48**, 10815 (1993).
[43] G. Schumm, Phys. Rev. B **49**, 2427 (1994).
[44] A. Merazga, H. Belgacem, C. Main, and S. Reynolds, Solid State Commun. **112**, 535 (1999).
[45] P. G. Lecomber, G. Willeke, and W. E. Spear, J. Non-Cryst. Solids **59-60**, 795 (1983).
[46] K. Shimakawa, J. Non-Cryst. Solids **266-269**, 223 (2000).
[47] J. Kočka, A. Fejfar, P. Fojtik, K. Luterova, I. Pelant, B. Rezek, H. Stuchlikova, J. Stuchlik, and V. Svrcek, Sol. Energy Mater. Sol. Cells **66**, 61 (2001), and references therein.
[48] J. Kocka, H. Stuchlikova, J. Stuchlik, B. Rezek, T. Mates, V. Svrcek, P. Fojtik, I. Pelant, and A. Fejfar, J. Non-Cryst. Solids **299-302**, 355 (2002), and references therein.
[49] J. Y. W. Seto, J. Appl. Phys. **46**, 5247 (1975).
[50] M. V. Garcia-Cuenca, J. L. Morenza, and J. Esteve, J. Appl. Phys. **56**, 1738 (1984).
[51] S. K. Ram, S. Kumar, R. Vanderhaghen, B. Drevillon, and P. Roca i Cabarrocas, Thin Solid Films **511-512**, 556 (2006).

[52] S. K. Ram, P. Roca i Cabarrocas, and S. Kumar, J. Non-Cryst. Solids **352**, 1172 (2006).
[53] S. K. Ram, P. Roca i Cabarrocas, and S. Kumar, Thin Solid Films **515**, 7576 (2007).
[54] Y. Lubianiker and I. Balberg, Phys. Rev. Lett. **78**, 2433 (1997).
[55] R. W. Collins, A. S. Ferlauto, G. M. Ferreira, C. Chen, J. Koh, R. J. Koval, Y. Lee, J. M. Pearce, and C. R. Wronski, Sol. Energy Mater. Sol. Cells **78**, 143 (2003).
[56] D. He, N. Okada, C. M. Fortmann, and I. Shimizu, J. Appl. Phys. **76**, 4728 (1994).
[57] X. Wang, Y. Bar-Yam, D. Adler, and J. D. Joannopoulos, Phys. Rev. B **38**, 1601 (1988).
[58] S. Y. Myong, O. Shevaleevskiy, K. S. Lim, S. Miyajima, and M. Konagai, J. Appl. Phys. **98**, 054311 (2005).
[59] S. Y. Myong, K. S. Lim, and M. Konagai, Appl. Phys. Lett. **88**, 103120 (2006).
[60] D. Han, G. Yue, J. D. Lorentzen, J. Lin, H. Habuchi, and Q. Wang, J. Appl. Phys. **87**, 1882 (2000).